

Hydrodynamical Models of Outflow Collimation in YSOs

Adam Frank ¹, Garrelt Mellema ²

arXiv:astro-ph/9606142v2 21 Jun 1996

¹ Hubble Fellow; Department of Astronomy, University of Minnesota, Minneapolis, MN 55455; e-mail: afrank@astro.spa.umn.edu

² Stockholm Observatory, S-13336 Saltsjöbaden, Sweden; email: garrelt@astro.su.se

In this paper we explore the physics of time-dependent hydrodynamic collimation of jets from Young Stellar Objects (YSOs). Using parameters appropriate to YSOs we have carried out high resolution hydrodynamic simulations modeling the interaction of a central wind with an environment characterized by a toroidal density distribution which has a moderate opening angle of $\theta_\rho \approx 90^\circ$. The results show that for all but low values of the equator to pole density contrast the wind/environment interaction produces strongly collimated supersonic jets. The jet is composed of shocked wind gas. Using analytical models of wind blown bubble evolution we show that the scenario studied here should be applicable to YSOs and can, in principle, initiate collimation on the correct scales ($R \lesssim 100$ AU). Comparison of our simulations with analytical models demonstrates that the evolution seen in the simulations is a mix of wind-blown bubble and jet dynamics. The simulations reveal a number of time-dependent non-linear features not anticipated in previous analytical studies. These include: a prolate wind shock; a chimney of cold swept-up ambient material dragged into the bubble cavity; a plug of dense material between the jet and bow shocks. We find that the collimation of the jet occurs through both de Laval nozzles and focusing of the wind via the prolate wind shock. Using an analytical model for shock focusing we demonstrate that a prolate wind shock can, by itself, produce highly collimated supersonic jets.

Animations from these simulations are available over the internet at WWW address <http://www.msi.umn.edu/Projects/twj/jetcol.html>

Subject headings: ISM: Jets and Outflows - hydrodynamics - star: formation

1. Introduction

The propagation of jets associated with Young Stellar Objects (YSOs) has been well studied both analytically (Raga & Kofman 1992) and with sophisticated numerical tools (Blondin, Fryxell & Königl 1990, Stone & Norman 1994a). These theoretical investigations, in conjunction with the growing data-base of high-resolution observations, have been extremely useful in understanding the hydrodynamics of HH jets and HH objects. The origin of these jets, however, remains an issue which has yet to be resolved. The obscuring dust and gas surrounding young stars has made it difficult to observationally determine physical conditions which can constrain collimation models for either the HH jets or the (perhaps related) bipolar CO outflows. In the absence of these constraints a number of collimation mechanisms have been proposed which, broadly speaking, fall into two categories: pure hydrodynamic models and magnetohydrodynamic models.

Many of the purely hydrodynamic studies produce well collimated supersonic outflows by invoking de Laval nozzles (Königl 1982, Raga & Cantó 1989). In these models an initially spherical stellar wind interacts with the surrounding medium and is shocked producing a high temperature cavity. If the walls of the cavity take on the appropriate “nozzle” configuration, transsonic solutions for the flow exist leading to the formation of a supersonic jet. There are, however, a number of problems with the de Laval nozzle scenarios. The nozzles in the cavity may be unstable (Koo & McKee 1992) and the high densities in the shocked gas may produce cooling distances too short to allow a “hot bubble” to form within the cavity (Pelletier & Pudritz 1992).

Another class of hydrodynamic collimation models which rely on the other extreme of cooling length scales was explored by Cantó (1980), Cantó & Rodriguez (1983) and Cantó, Tenorio-Tagle & Rozyczka (1988). In these models strong radiative losses create a thin aspherical shell. After the freely expanding wind strikes the shock at an oblique angle it is redirected to flow along the walls of the shell. At the vertex of the aspherical (prolate) shell a converging conical flow is established which produces a jet. The main problem with these models is the size scale of the steady-state shell (based on achieving pressure equilibrium) which is larger than the size of observed collimation regions ($R \approx 100$ AU, see Burrows & Stapelfeldt 1995).

The strong evidence supporting circumstellar disks (Strom 1994) and magnetic fields around T Tauri stars has led to a different set of scenarios for producing well collimated jets. In these MHD “disk-wind” models the outflows are centrifugally driven by a magnetized accretion disk. Considerable effort has gone into the theory that the magnetic field in the disk forces the accreting gas into co-rotation. Centrifugal acceleration and magnetic force

then lift the gas off the disk producing a wind which is eventually collimated into a jet as the field lines bend back towards the disk/star rotation axis (Königl 1989, Pudritz 1991). The details of the gas acceleration depend on the magnetic field configuration (Pelletier & Pudritz 1992, Todo *et al* 1993, Wardle & Königl 1993, Holland *et al* 1995), the star-disk interaction at the boundary layer (Camenzind 1993, Najita & Shu 1994), and the stability in co-rotation (Uchida & Shibata 1985). These disk-wind models are very promising and the current consensus appears to be that the outflow collimation occurs through some kind MHD process. However, these models also have their problems. MHD disk-wind models suffer from difficulties in producing the correct disk-field orientations (Shu 1991). Other magneto-gasdynamic models suffer from uncertainties in the actual field strengths and orientations achieved in YSOs (Balbus 1993, Goodman *et al* 1990, Heyer *et al* 1987). In addition it is not clear if or how long the field can maintain the focusing of the flow into a tightly collimated jet or if the collimation can be achieved on the correct scales (Stone & Norman 1994b).

To further complicate matters there is now increasing observational evidence that that collimated YSO flows are *essentially* unsteady. HH jets show signs of velocity variations (Morse *et al.* 1992) and entrainment (Hartigan *et al* 1992), suggesting that both the driving of the YSO wind and its interaction with the circumstellar environment are time-dependent processes.

Clearly a great deal of progress remains to be made in our understanding of the YSO collimation process. Because of the complexity of both the flows and the underlying physics, numerical simulations are an effective tool for studying outflow collimation. While there is an abundance of simulations of fully developed jets (Blondin, Fryxell & Königl 1990, Stone & Norman 1994a) surprisingly little numerical work has been done on their collimation or on the collimation of the bipolar outflows (see e.g. Norman 1993, Chernin & Masson 1994). In this paper we seek to re-examine gasdynamical collimation using high-resolution numerical simulations. Recent numerical studies of the formation of Planetary Nebulae have shown that excellent collimation can be achieved through the interaction of a spherical central wind with a toroidal circumstellar environment (Mellema, Eulderink & Icke 1991, Icke, Balick & Frank 1992, Icke *et al* 1992). These studies have demonstrated that nonlinear and time-dependent gasdynamic effects provide collimating mechanisms which were unanticipated or not fully appreciated in previous analytical models. The time-dependent collimation processes have been named 'Shock-Focused Inertial Confinement' (SFIC). In the SFIC mechanism the interaction of the inertia of a toroidal environment with the thermal pressure of the shocked wind produces a well collimated jet.

In a preliminary study Frank & Noriega-Crespo 1994 (hereafter FN94) investigated

the SFIC mechanism in the context of YSOs. FN94 used a toroidal density environment which included an accretion flow. Their simulations showed that focusing at the inner shock could produce strongly collimated supersonic flows. While these results are promising a deeper understanding of the SFIC mechanism is required before a serious application to YSO jets can be attempted. In this paper we attempt to take some steps in this direction by investigating an idealized adiabatic version of SFIC collimation. Using numerical simulations and analytical estimates we will attempt to further identify the basic processes at work in SFIC collimation and put limits on their applicability to YSOs.

In re-examining hydrodynamic collimation our intent is not to try to push MHD models aside. There are many reasons for expecting magnetic fields to be important in producing at least some jets, particularly those associated with T Tauri stars. But a robust model of hydrodynamic collimation could be used to produce jets even in those cases where the MHD scenarios such as the disk-winds models can produce only poorly collimated winds or where MHD collimation is not effective on all scales relative to the full length of the jet. We note that the hydrodynamics we explore in this paper has elements similar to both Cantó's 1980 model and de Laval nozzles. Thus we intend to study the SFIC mechanism as a general set of processes which may individually operate in some form across a variety of length scales rather than as the definitive model for the production of YSO jets. We note here that since we are exploring the effect of the circum-protostellar environment on jet formation our models may be particularly relevant to the more deeply embedded class 0 objects.

The organization of the paper is as follows: In section II we describe of the numerical method and initial conditions used in our simulations. In Section III we provide some analytical estimates of the range of applicability of the SFIC mechanism with respect to initial conditions. In section IV we examine the results of our numerical models. In section V we explore the collimation mechanisms seen in the simulations. Finally in section VI we present our conclusions along with a discussion of some issues raised by the simulations.

2. Numerical Method and Initial Conditions

The numerical model (initial conditions and governing equations) we have constructed for our simulations capture the essential characteristics of the environment we wish to study: a central wind interacting with a toroidal environment. Our ultimate goal is to investigate the collimation of realistic YSO jets through the SFIC mechanism described in section I. But in this paper, we focus on the physics of SFIC collimation in an idealized environment. We state explicitly that the initial conditions used here are not meant to

be realistic in the sense of modeling an actual YSO environment. There are a number of scenarios for gravitational collapse that lead to star formation: collapse of a rotating spherical cloud (Tereby, Shu & Cassen 1984); collapse of a spherical cloud threaded by an ordered magnetic field (Galli & Shu 1993); collapse of a flattened filament (Hartmann *et al.* 1994). Each of the collapse scenarios listed above would produce a toroidal density distribution. However, the explicit form of those distributions as well as the form of the velocity fields they create would vary considerably from one scenario to the next. Since we intend to study the SFIC mechanism in the context of specific collapse scenarios in a future work, we use here their common characteristics as initial conditions for the environment.

The gasdynamic interactions we wish to study are governed by the Euler equations. In our numerical model we express these in azimuthally symmetric cylindrical coordinates:

$$\frac{\partial \rho}{\partial t} + \frac{1}{r} \frac{\partial \rho u_r}{\partial r} + \frac{\partial \rho u_z}{\partial z} = 0, \quad (2-1)$$

$$\frac{\partial \rho u_r}{\partial t} + \frac{1}{r} \frac{\partial \rho u_r^2}{\partial r} + \frac{\partial \rho u_r u_z}{\partial z} = -\frac{\partial p}{\partial r} \quad (2-2)$$

$$\frac{\partial \rho u_z}{\partial t} + \frac{1}{r} \frac{\partial \rho u_z u_r}{\partial r} + \frac{\partial \rho u_r^2}{\partial z} = -\frac{\partial p}{\partial z}, \quad (2-3)$$

$$\frac{\partial E}{\partial t} + \frac{1}{r} \frac{\partial (E+p)u_r}{\partial r} + \frac{\partial (E+p)u_z}{\partial z} = 0, \quad (2-4)$$

and

$$E = \frac{1}{2} \rho (u_r^2 + u_z^2) + \frac{1}{(\gamma - 1)} p, \quad (2-5)$$

where the terms have their usual meaning. To solve these equations we use the Total Variation Diminishing (TVD) method of Harten (1983) as implemented by Ryu *et al* (1995). TVD is an explicit method for solving hyperbolic systems of equations. It achieves second order accuracy by finding approximate solutions to the Riemann problem at each grid boundary while remaining non-oscillatory through the application of a lower order monotone scheme. The implementation of the TVD method used here is robust and requires even less CPU time than older methods such as the Flux Corrected Transport (FCT) schemes (Boris & Book 1973).

Note that equations 2-1 through 2-5 do not include the effects of rotation and gravitational fields. We also leave out the effects of radiative energy losses. As said at the beginning of this section, we focus here on the simplest case, the purely adiabatic, purely gas dynamical collimation of jets. As we shall demonstrate, even under these constraints the flow pattern which develops is quite complex. We feel it is important to understand the dynamics of these flows before adding additional physics. Below we provide some

justification for ignoring the effects of gravity and rotation and in section 3 we discuss the potential role of radiative cooling in our collimation mechanisms.

The most important feature of the environment for this study is the presence of a initial density contrast between pole and equator. Because gravity and rotation can both determine the shape of the density distribution we will use a toroidal density distribution with a radial power law appropriate to an in-falling cloud in the central potential of a protostar. The initial density distribution we chose to work with takes the following form:

$$\rho(R, \theta) = \frac{\dot{M}_a}{4\pi R^2} \left(\frac{2GM}{R}\right)^{-\frac{1}{2}} \left\{1 - \frac{\zeta}{6} [13P_2(\cos(\theta)) - 1]\right\} \quad (2-6)$$

Note that eq 2-6 is expressed in spherical coordinates. In the rest of this paper we will use R and r to denote the spherical and cylindrical radii respectively where $R = \sqrt{r^2 + z^2}$ and $\theta = \tan^{-1}(r/z)$. In eq 2-6 \dot{M}_a is the accretion mass loss rate and M is the mass of the star. Equation 2-6 is a modified form of eq 96 from Tereby, Shu & Cassen 1984 (originally derived by Ulrich 1976). We use it here because produces the required toroidal geometry as well having the $R^{-\frac{3}{2}}$ radial dependence, appropriate to a freely falling envelope. The parameter ζ , which determines the flattening of the cloud, is normally a function of radius (due to conservation of angular momentum). Since one of the principal goals of this study is to isolate the effect of the equator to pole density contrast ($q = \rho_e/\rho_p$) on the SFIC collimation process we have modified the original equation making ζ constant and treating it as an input parameter. Also in collapse schemes like that described Hartmann *et al.* 1994 in which there is no rotation the pole to equator density contrast will not be a strong function of radius. The relation between ζ and q is

$$q = \frac{12 + 15\zeta}{12 - 24\zeta}. \quad (2-7)$$

In the present application we set the velocity in the environment equal to zero to allow comparison with analytical predictions. In reality the cloud will be falling inward at velocities on the order of $v_g \approx \sqrt{GM/R}$. Gravity and the infall motions of the cloud are, of course, the most important physical components that actually form the star. However, we ignore these aspects of the problem in the present study because the outward velocities produced by the wind/environment interaction are much greater v_g and our goal is understanding the more restricted problem of hydrodynamic jet collimation dynamics. In this study we are more interested in the formation of the jets than in the formation of the star. Thus we can ignore the dynamical effect of the infall velocity. Although the condition $v_o \gg v_g$ does not hold for all shock positions (as we will see the equatorial shock moves out very slowly), we found in tests that neglecting the accretion velocity does not make a substantial difference for the bubble structure. A similar argument can be made with

respect to rotational velocities since infalling material must rotate at speeds less than the Keplerian value.

In Fig 1 we present a contour plot of the density distribution given by eq 2-6. Superimposed on top of the density contours we plot a line marking the full-width half maximum of the distribution, i.e. the angle at which the density falls by half its value at the equator. Note that the “opening angle” of the torus defined in this way is $\sim 90^\circ$. Thus while our initial conditions do not describe a thin disk they certainly do not correspond to “funnels” either and one would not, *a priori*, expect them to produce collimated jets.

We assume that the temperature in the cloud is constant. The ambient pressure is then set by the equation of state for an ideal gas. Note that this implies an outward pressure gradient in the environment. But the low temperatures in the environment ($T < 500$ K) ensure small values for the sound speed and we do not see appreciable evolution of the environment during a simulation.

The initial conditions for the spherically symmetric central wind are fully specified by its mass loss rate \dot{M}_w , velocity V_w , and temperature T_w . In the simulations the wind is fixed in a spherical region ($R < R_o$) at the center of the grid. The use of cylindrical (r, z) coordinates prohibits exact specification of the inner wind “sphere” and produces a staircase-like pattern. This leads to small oscillations in the temperature and velocity of the freely flowing wind. To check that these effects do not degrade the computed solutions we have compared our simulations of both spherical and aspherical wind blown bubbles with analytical models (Weaver *et al.* 1977, Koo & McKee 1992) as well as simulations computed with other numerical methods in spherical coordinates (Frank 1992). We find no appreciable effects of the imperfect inner wind boundary on the bubble dynamics. The numerical simulations reproduced the self-similar analytical models usually to better than 10%, but never worse than 15% in terms of shock radii and velocities.

We have run over 30 simulations exploring a variety of initial parameters. In this paper we present the results of eight of these. Their input parameters are listed in Table 1.

3. Applicability to YSOs

The SFIC mechanism produces jets inside wind-blown bubbles with the well-known ‘three shock’ structure. The first shock faces outward into the environment and is often called the “outer” shock. Following Koo & McKee 1992 we refer to this structure as the “ambient shock” (R_s). The second shock faces into the central wind. It is responsible

for decelerating and heating the wind. In the literature it is sometimes referred to as the “inner” or “reverse” shock. We call it the “wind shock” (R_{sw}). Between these two shocks is the contact discontinuity (CD) separating the shocked wind gas from the shocked ambient gas.

Previous simulations of SFIC collimation have shown that “flow focusing” at the wind shock is an important process for collimating SFIC jets. When the spherical wind strikes the aspherical wind shock at an oblique angle it is partly redirected into a beam aligned to the poles of the toroidal density distribution. Since the focusing occurs *inside* the wind-blown bubble the wind and ambient shocks must be well separated if the SFIC mechanism is to be effective. A similar argument holds for the presence of de Laval nozzles where the shocked wind fills a cavity that acts as a reservoir of thermal energy to be converted into bulk kinetic energy of a jet. Thus a necessary condition for the hydrodynamic collimation mechanisms studied here to be effective is that $R_s \gg R_{\text{sw}}$ over at least the polar sector of the wind-blown bubble. Using simple analytical estimates we demonstrate below that it is possible to obtain this condition and, in principle, achieve hydrodynamic collimation through either/both de Laval nozzles and/or the SFIC mechanism on scales that are consistent with YSO observations.

A shock wave is called radiative if the cooling time for the post-shock gas is shorter than the dynamical time scale for its evolution. If both the wind and ambient shocks are fully radiative then their separation will be small. Thermal energy gained at the shocks is quickly radiated away and, lacking pressure support, the shocked wind and shocked ambient material collapse on to each other forming a thin dense shell. The bubble will then be driven by the momentum of the wind. Given a sufficient equator to pole density contrast in the ambient medium, a momentum driven bubble will become highly aspherical. Just as in the SFIC mechanism described above, the wind in an aspherical radiative bubble will strike the inner shock at an oblique angle causing focusing towards the poles. In this situation, however, the shocked wind material must slide along the inner edge of the thin shell and can only form a jet directly over the poles were its conical stream converges. Such a configuration was the basis of Cantó’s 1980 model for the production of HH objects (see also Tenorio-Tagle, Cantó & Rozyczka 1988). Numerical simulations of the SFIC mechanism with radiative cooling included also produce this type of flow pattern (Mellema & Frank 1996a, Mellema & Frank 1996b).

When the cooling time for the shocked wind t_c is comparable to, or longer than, the dynamical time scale for the bubble’s evolution t_d , the post-shock wind does not lose its thermal energy to radiation and has enough pressure to push the wind and ambient shocks apart. A hot cavity of shocked wind material forms, filling a large fraction of the bubble’s

volume. The swept-up shocked ambient material, however, remains confined to relatively thin shell. This is the domain where collimation through de Laval nozzles and the SFIC mechanism is possible. The bubble is said to be “energy conserving” or “adiabatic”.

If we wish to determine where in YSO parameter space SFIC jets might form, we must determine the radii at which the shocks in a wind-blown bubble begin to separate. The usual means of doing this is to determine the radius at which a bubble makes a transition from being radiative (or momentum driven) to being adiabatic (or energy driven). There is, however, another possibility.

In their work on the evolution of wind blown bubbles Koo & McKee 1992 showed that between the radiative and adiabatic configurations lies another evolutionary state which they called the Partially Radiative Bubble (PRB). In a PRB the cooling time for the gas is shorter than the age of the bubble but longer than the time it takes for the unshocked wind to reach the wind shock i.e. $t_{\text{cross}} < t_{\text{cool}} < t_{\text{d}}$ where $t_{\text{cross}} = R_{\text{s}}/v_{\text{w}}$. While at any time in the PRB stage most of the shocked wind will have cooled, the wind material which has recently past through the shock will still be hot enough to keep $R_{\text{s}} \gg R_{\text{sw}}$. Thus the appropriate transition radius we must find is $R_{\text{t}}(\text{PRB})$: the distance at which a radiative bubble makes the transition to a PRB.

Of course not all bubbles will make a transition to the PRB stage. But as long as the radial density distribution is such that

$$\rho(r) = \rho_{01} r^{-k}, \quad (3-1)$$

the range of accretion rates \dot{M}_{a} , wind mass loss rates \dot{M}_{w} and wind velocities v_{w} appropriate for YSOs, is such that all wind-blown bubbles with $k = 3/2$ will enter the PRB phase. Below we calculate the PRB transition radius $R_{\text{t}}(\text{PRB})$.

The expansion of a radiative, momentum-driven bubble into an environment given by eq 3-1 is

$$R_{\text{s}} = \left(\frac{(3-k)\dot{M}_{\text{w}}v_{\text{w}}}{12\pi\rho_{01}} \right)^{\frac{1}{4-k}} \left(\frac{t}{a} \right)^{\frac{2}{4-k}}, \quad (3-2)$$

where R_{s} is the radius to the outer shock, and $a = \sqrt{2/(12-3k)}$. The cooling time for post shock gas t_{c} can be estimated from the familiar results of Kahn (1976)

$$t_{\text{c}} = \frac{Cv_{\text{s}}^3}{\rho_{\text{pre}}}, \quad (3-3)$$

where $C = 6 \times 10^{-35} \text{ g cm}^{-6} \text{ s}^4$ and ρ_{pre} is the preshock density. By setting $t_{\text{cool}} = t_{\text{cross}}$ and

using eqs 3-1 through 3-3 Koo & McKee 1992 derived the transition time scale

$$t_t(\text{PRB}) = \sqrt{\left[\frac{1}{4\pi C}\right]^{4-k} \frac{12\pi\rho_{01}a^2}{(3-k)} \dot{M}_w^{(3-k)} v_w^{-(21-5k)}}. \quad (3-4)$$

Substituting this into equation 3-2 gives

$$R_t(\text{PRB}) = \left(\frac{1}{4\pi C}\right) \dot{M}_w v_w^{-5}. \quad (3-5)$$

Note that while $t_t(\text{PRB})$ depends on k and ρ_{01} , $R_t(\text{PRB})$ does not. Note also the strong dependence of $R_t(\text{PRB})$ on velocity.

For comparison let us also calculate $R_t(\text{AD})$, the radius at which the bubble becomes fully adiabatic. Koo & McKee 1992 calculate the time scale for a PRB to become an adiabatic bubble but it depends on γ_{sw} the ratio of specific heats in the PRB's shocked wind. Since this quantity cannot be calculated in a straight forward way we will derive $R_t(\text{AD})$ by equating the age of a momentum driven bubble with the cooling time for the post-shock wind $t_c = t_d$. In this case eq 3-3 takes the form

$$t_c \approx \frac{4\pi C v_w^4 R_s^2}{\dot{M}_w}. \quad (3-6)$$

In eq 3-6 we have assumed that the shock velocity v_s is approximately equal to the wind velocity v_w . Inverting eq 3-2 gives a dynamical time t_{dyn} . Using this we find,

$$R_t(\text{AD}) = \left(\frac{a}{4\pi C}\right)^{\frac{2}{k}} \left(\frac{12\pi\rho_{01}\dot{M}_w}{3-k}\right)^{\frac{1}{k}} v_w^{-\frac{9}{k}}. \quad (3-7)$$

In Fig 2 we show $R_t(\text{PRB})$ and $R_t(\text{AD})$ versus v_w for $\dot{M}_w = 10^{-7} M_\odot \text{ yr}^{-1}$. The curve for $R_t(\text{AD})$ was calculated using $\dot{M}_a = 10^{-6} M_\odot \text{ yr}^{-1}$ and $k = 3/2$. Figure 2 demonstrates that the bubble enters the partially radiative stage at $R < 100 \text{ AU}$ for $v_w > 150 \text{ km s}^{-1}$. The results of Hirth *et al* 1994 and recent HST images (Burrows & Stapelfeldt 1995) give sizes for the collimation region on the order of 100 AU. In addition most HH jets are observed to have velocities on the order of 200 km s^{-1} or more. In a collimation model that relies on either shock focusing or de Laval nozzles these jet speeds imply even higher wind speeds. Thus Fig 2 shows that the shock configurations needed for hydrodynamic collimation are expected to begin to operate with initial parameters and on size scales compatible with those derived for YSOs.

4. Results

4.1. Basic Flow Pattern

In this section we focus on the results of a single jet producing simulation: case A in Table 1. At the end of this section we explore the role of initial conditions on the final flow. For now we note that while the density contrast used in case A is high ($q = 70$) the features seen are characteristic of all the other simulations where jets appear ($q \geq 7$). In Figs 3 and 4 we present results of the case A simulation after 1035 years of evolution. Figure 3 shows a gray scale map of the logarithm of the density alongside of a vector map of the velocity field. Figure 4 shows gray scale maps of both temperature and pressure. Note that the darkest gray tones in Fig 3 correspond to low values of the density, whereas in Fig 4 the darkest gray tones correspond to high values of temperature and pressure.

Figures 3 and 4 demonstrate that the central wind, emerging from the base of the grid, becomes highly focused through the interaction with the environment. While there are features of the overall flow pattern that resemble a wind blown bubble, the shocked wind has clearly been collimated into a supersonic jet. The collimation can be most clearly seen in the velocity vectors in Fig 3. These show a high speed flow above (behind) the wind shock, aligned with the z axis.

In order to understand the nature and origin of the flow pattern we focus first on the density map. In the parlance of wind-blown bubble theory discussed in section 3 we can define the outer boundary of the interaction region or “bubble” by the shock wave driven into the ambient medium by the central wind. Behind this ambient shock is a shell of swept-up, compressed ambient gas. At any height z the highest densities in the flow are found in this shell. The inner boundary of the bubble is defined by the shock wave which faces into the central wind, decelerating and heating it. It is the mildly aspherical feature at the base of the computation domain surrounding the freely expanding spherical wind.

Ignoring the flow interior to the swept-up shell for the moment, the elongation of the bubble can, to first order, be explained in a simple way. Note first that the ambient pressure can play no role in shaping the bubble. The highest pressures in environment are achieved in the equator where $P_e \propto \rho_e T_e$. Even there the pressure there is always orders of magnitude lower than the driving thermal pressure achieved in the shocked wind with $P_{sw} \propto \rho_w v_w^2$. Thus only the inertia of the environment affects the shape of the bubble. In his study of wind blown bubble dynamics Icke (1988) used Kompaneets’ (1960) formalism to derive an expression for the evolution of the ambient shock,

$$R_s = R_s(\theta, t) \tag{4-1}$$

$$\frac{\partial R_s}{\partial t} = \left\{ A \left(1 + \left(\frac{1}{R_s} \frac{\partial R_s}{\partial \theta} \right)^2 \right) \right\}^{\frac{1}{2}} \quad (4-2)$$

where

$$A = \frac{\gamma + 1}{2} \frac{P_{sw}}{\rho_{01}(\theta)} \quad (4-3)$$

Equation 4-2 shows that $A = A(\theta)$ can be defined as a local acceleration parameter for the ambient shock. Therefore the run of $A(\theta)$ determines the asphericity of the bubble. Since the Kompaneets approximation assumes that P_{sw} is constant across the shocked wind cavity it is the environments density distribution (inertia) which determines the θ dependence of A .

The flow of shocked wind interior to the swept-up shell departs strongly from the expectations of wind-blown bubble theory. According to the classic theory of non-radiative wind-blown bubbles the flow of the hot shocked wind should be subsonic at a high uniform pressure P_{sw} . But the density map in Fig 3 shows at least two sharp discontinuities at heights $z = 8 \times 10^{16}$ cm and $z = 1.35 \times 10^{17}$ cm in the shocked wind cavity. Comparison of the velocity, temperature and pressure maps show that these features are strong shock waves, which means that the flow in the cavity has been accelerated to supersonic speeds. Thus it is no longer appropriate to interpret the dynamics in the simulations purely in terms of energy driven wind-blown bubbles. Instead we have a situation which is a mix of jet propagation and bubble evolution physics.

These “internal” shocks in the cavity are quite consistent with theory of supersonic jets. It is well known that the interaction of a jet with the surrounding medium will produce two shocks: a bow-shock facing into the environment; and a jet-shock facing upstream into the oncoming jet material (Norman 1993). Consideration of the pressure map in Fig 4 demonstrates that the leading discontinuity at height $z = 1.35 \times 10^{17}$ cm can be identified as the the jet shock. Indeed, the shock configuration is consistent with a Mach-disk as is expected for a terminal jet shock. The second “internal” shock wave in the body of the jet at $z = 8 \times 10^{16}$ cm also has a Mach disk configuration. The origin of this feature is consistent with the crossing shocks expected in the propagation of an initially over pressured jet (Norman 1993).

The bubble’s ambient shock appears to double as a bow shock for the collimated jet. This dual-identity is another manifestation of the mix between jet and bubble dynamics. Examination of animations, (which can be seen at the WWW site <http://www.msi.umn.edu/Projects/twj/jetcol.html>), as well as plots of the various quantities along the axis (see Fig 5), show the region between the jet and ambient/bow

shocks to be more complex than might be expected for a simple jet/environment interaction. From the maps shown in Figs 3 and 4 one can see a structure in this region that resembles a kind of oblong plug not seen in previous jet simulations. We note that simulations driving a jet into this kind of stratified environment have yet to be performed (see Dal Pino 1995 for examples of jet propagation simulations in non-constant environment). We will return to the origin and evolution of the jet head or “plug” in the next sub-section.

Another feature of the simulations expected from standard jet physics is the cocoon of “waste” material shed by the jet across the sides of Mach disk (Norman 1993). This material is first decelerated by the jet shock and then is diverted to flow back around the side of the jet body. In our simulations there is an additional feature associated with the propagation of the jet and the cocoon. Note the presence of a relatively cool but dense tongues of shocked ambient material that extends from the CD at $z \approx 5 \times 10^{16}$ cm into the shocked wind cavity. Given the cylindrical symmetry of these simulations this feature acts like a chimney surrounding the jet and helps to maintain its collimation. Such chimneys have been observed in other SFIC simulations and they appear to be an important element of the inertial confinement collimation mechanism (Mellema, Eulderink & Icke 1991, Icke, Balick & Frank 1992, FN94).

To assist in identifying the basic features of the simulations in Fig 5 we present cuts along the z axis of the density, velocity, pressure and Mach number. The wind shock and ambient/bow shock can be recognized in all variables at $z \approx 1000$ and 12500 AU respectively. Similarly the jet-shock and internal Mach disk are apparent at $z \approx 6000$ and 9000 AU. Note that the Mach number is frame dependent and the distinction between subsonic and supersonic flows is sensible only in the frame of a particular shock wave. Detailed examination of the evolution of the wind shock shows that it progresses very slowly. Its rest frame and the frame defined by the stationary grid are essentially identical and the Mach numbers shown in Fig 5 are only correct for the flow between the wind shock and the internal Mach disk.

In Fig 3 note first that the flow is clearly being accelerated from subsonic to supersonic velocities ($\mathcal{M} \approx 3$) *after* passing through the wind shock. This suggests the presence of a de Laval nozzle. Note also that the average density in the body of the jet, which we define to be the region between the wind shock and jet-shock, is $\langle n \rangle \approx 100 \text{ cm}^{-3}$ which is lower than the density in the environment. Thus our simulations are producing light supersonic jets (i.e $\eta = \rho_e/\rho_j < 1$). However, since the environmental density will continue to decline with distance the jet will eventually become “heavy”, ($\eta > 1$), if the simulations were to be continued on a larger grid for a longer time. In a real protostellar environment the jet would probably meet the edge of the cloud before that happened and the jet would become heavy

more abruptly. The addition of radiative cooling will remove lateral pressure support for the jet and should allow it to collapse to smaller widths and higher densities (Raga & Cantó 1989). Thus we expect the jets produced in our simulations will always become heavy at some point. Finally, note again the complicated structure in the “plug”, the region between the jet-shock and the ambient/bow shock. We will return to this point in the next section.

The continuing collimating effect of the environment can be seen by considering the opening angle of the jet. The opening angle of a freely expanding supersonic jet depends on its Mach number,

$$\phi = 2 \tan^{-1}\left(\frac{1}{\mathcal{M}}\right) \quad (4-4)$$

From equation 4-4 the jet shown in Figs 3 and 4 would, if unconstrained, have an opening angle of at least 40° . An opening angle of $\phi \approx 22^\circ$ appears more appropriate to the simulation, indicating that continuing confinement by the chimney and the swept-up shell are important in the dynamics of the jet.

4.2. Evolution

Our simulations demonstrate that a well collimated supersonic jet develops from the evolution of a wind-blown bubble, the system being an interesting mix of both wind-blown bubble and jet dynamics. We have already identified the ambient and wind shocks appropriate to wind-blown bubbles and the jet shock, crossing shocks and cocoon of waste jet gas appropriate to jets. In order to make the evolution of these features more explicit we present in Fig 6 the evolution of the system through seven sequential gray scale maps of the density, taken every 147 years.

There are a number of noteworthy features in Fig 6. Firstly the evolution of the wind shock: as the system evolves it becomes more and more aspherical, prolate geometry. Using the distance to wind shock in the pole $R_{sw}(P)$ and equator $R_{sw}(E)$ we can define an ellipticity parameter to describe its geometry,

$$e = \frac{R_{sw}(E)}{R_{sw}(P)}. \quad (4-5)$$

Detailed examination of the wind shock shows that after 200 years of evolution it assumes a quasi-steady configuration with an ellipticity of $\langle e \rangle \approx .75$. As we will see the asphericity of the wind shock plays an important role in the collimation of the flow (Sect 5.3).

Capturing the wind shock poses special challenges for the numerical code as it is strong and extends over a relatively small region. One of the disadvantages of using a cylindrical code is the difficulty in modeling quasi-spherical structures on a small number of grid points. At later times in the evolution of the models we find that numerical errors appear in the wind shock. These are apparent in the small “flame” shaped region of low density immediately behind the wind shock and close to the symmetry axis. By viewing animations of the simulation we have found that this feature produces a small but noticeable effect on the evolution of the jet. The distortion of the wind shock drives a periodic modulation in the post-shock velocity. The pulses can be seen in velocity plot shown in Fig 5. Fig 6 shows that until $t \approx 900$ years there is a crossing shock in the jet at a distance about $z \approx .5R_{\text{sw}}(\text{P})$, which can be explained as the expansion and subsequent contraction of an overpressured jet (Norman 1993). The velocity pulses produced at the wind shock however change the crossing shock into an “internal” Mach-disk, a structure of similar character and origin to the internal working surfaces explored by Biro & Raga 1994.

Fig 6 also demonstrates the role of the collimating chimney. As the system evolves relatively cool and dense shocked ambient gas is continually pulled off the CD. This material is driven upwards into the shocked wind cavity where its inertia helps maintain the collimation of the jet. Comparison of Figs 3 and 4 shows the correlation between pressure in the jet and the shape of the chimney. The kink in the chimney occurs at roughly the same height as the crossing shock.

In order to test the sensitivity of the chimney structure to numerical viscosity we did a series of simulations with increasing resolution. We doubled the resolution from 64×320 through 256×1280 . Each grid doubling reduces the numerical viscosity by a factor of 4. Reducing the viscosity in this way did not effect the existence or evolution of the chimney other than steepening the density gradients. Due to constraints on computational time we have not, however, been able to continue the grid doubling and we can not at this time say that our simulations are fully converged.

The physical origin of the chimney appears to be Kelvin-Helmholtz instabilities at the CD. Near the base of the flow a large shear gradient exists between the shocked wind and the shell of shocked ambient gas as can be seen in the velocity map in Fig 3. Detailed inspection of animations shows that the chimney develops when corrugations in the CD (assumed to originate from KH instabilities) are convected up by the bulk flow in the shocked wind cavity.

Some aspects of the evolution of the “plug” at the head of the jet can also be followed in Fig 6. Consideration of this figure and density plot in Fig 5 shows that there are two contact discontinuities in the plug. In Fig 5 these occur at $z \approx 9500$ and $z \approx 12000$ AU

respectively. From Fig 5 it can be seen the contact discontinuity occurring at $z \approx 12000$ AU is the inner edge of the swept-up shell of ambient gas. The contact discontinuity at $z \approx 9500$ AU marks the contact discontinuity at inner edge of what would be, in a classic jet, the bow shock. In our simulations however much the material between these two contact discontinuities originates in the stellar wind. From inspection of the early epochs of the simulations it appears that the plug initially forms from subsonic material injected into the shocked wind cavity before the jet forms. This material entered the cavity at relatively high densities and was then further compressed by the jet once it develops. At later times however Fig 3 and 6 show that additional material is added to the plug as shocked jet gas exiting the Mach-disk “splatters” against the shell and is driven both backward into the cocoon and forward into the plug. Ambient material appears to be pulled into the plug at these points as well during the later evolution of the jet/bubble.

The mixture of wind-blown bubble and jet dynamics can be quantitatively explored by examining the evolution of three characteristic lengths: the distance to the ambient shock along the pole $R_s(\text{P})$; the distance to the ambient shock along the equator $R_s(\text{E})$; the radius of the wind shock R_{sw} . Recall that $R_{\text{sw}}(\text{P}) \approx R_{\text{sw}}(\text{E})$. For a spherically expanding bubble both $R_s(t)$ and $R_{\text{sw}}(t)$ have closed form analytical expressions.

$$R_s(t) = \lambda_1 \left[\frac{\dot{M}_w v_w^2}{\rho_{01}} \right]^{\frac{2}{7}} t^{\frac{6}{7}}. \quad (4-6)$$

$$R_{\text{sw}}(t) = \lambda_2 \left[\frac{\dot{M}_w v_w^{\frac{5}{6}}}{\rho_{01}} \right]^{\frac{3}{7}} t^{\frac{11}{14}}. \quad (4-7)$$

where both λ_1 and λ_2 are constants of order 1. Exact expressions for these quantities can be found in Koo & McKee 1992. We focus first on the growth of the ambient shock. In Fig 7 the evolution of both $R_s(\text{P})$ and $R_s(\text{E})$ is plotted at 100 years intervals. In addition we have also plotted the growth expected for these shocks if $R \propto t^{\frac{6}{7}}$. These curves have been normalized to the time and distance of the first plotted point. Along the pole the ambient shock is clearly expanding faster than the predicted $t^{\frac{6}{7}}$ rate while long the equator it expands slower than predicted. The inner shock is also expanding more slowly than its predicted rate of $t^{\frac{11}{14}}$. The points plotted with an asterisk are the analytical predictions for the magnitudes of $R_s(\text{P})$, $R_s(\text{E})$ and R_{sw} respectively at $t = 900$ years. These values were calculated using the appropriate mass loss rates along the equator and the pole. Recall that the simulations of spherical bubbles recovered both the predicted rates and magnitudes to within 10%. While we do not expect spherical models to recover the magnitudes of aspherical bubbles the growth rates should be well matched (see Dwarkadas *et al* 1995). From Fig 6 however it is clear that none of these quantities is recovering the analytical growth rates for a wind blown bubble and only R_{sw} is within the systematic errors of the predicted magnitude.

Consideration of the ambient shock velocity along the pole V_{sp} is also useful in determining the dynamics of the system. The velocity of a jet bow shock is given by the familiar formula

$$V_{\text{bs}} = V_{\text{jet}}(1 + \sqrt{\eta})^{-1}. \quad (4-8)$$

If $R_s(\text{P})$ evolved solely as a jet bow shock, then

$$V_{\text{sp}}(R) = V_{\text{bs}}(z) = V_{\text{jet}}\left(1 + \sqrt{\eta} \frac{1}{z^{\frac{3}{4}}}\right)^{-1} \quad (4-9)$$

where

$$\eta = \frac{\rho_{01}}{\rho_j}. \quad (4-10)$$

Thus the ambient shock would accelerate along the pole. If $R_s(\text{P})$ evolved solely as wind blown bubble then

$$V_{\text{sp}}(R) \propto \left[\frac{\dot{M}_w v_w^2}{\rho_{01}}\right]^{\frac{1}{3}} R_s^{-\frac{1}{6}} \quad (4-11)$$

and the ambient shock would decelerate along the pole. The lower right hand panel of Fig 7 shows the actual velocity in the simulations as a function of radius. For comparison we have also plotted representative curves for both the evolution of a jet bow shock and a wind blown bubble. Apart from small variations, the velocity is roughly constant at $v_{\text{sp}} \approx 60 \text{ km s}^{-1}$. Thus the simulations indicate that in spite of the clear presence of a jet the global dynamics of the system lies between that of a pressure driven bubble and supersonic jet.

4.3. Collimation and Initial Conditions

In order to test the limits of the hydrodynamic collimation mechanisms under study we have explored the parameter space of initial conditions for the simulations. We find that the density contrast q is the most important parameter for determining the collimation of the flow. In Fig 8 we show contour plots of density from four different simulations (case C, D, E and F) each with different initial values of the equator to pole contrast q ($q = 3, 7, 14$ and 30 respectively). These plots demonstrate that collimation of the shocked wind flow into a jet occurs between $q = 7$ and $q = 14$. These are not extreme values. The values of q obtained in numerical simulations of the collapse of rotating clouds can be as high as 1000 (Yorke *et al.* 1993). Recall also that the collimation of the flow occurs without the benefit of additional ram pressure from the inward directed accretion flow that would occur with more realistic initial conditions. Since the accretion velocity goes as $R^{(-\frac{1}{2})}$ the asphericity which develops from the density gradient will be enhanced as the equatorial shock will

remain at relatively smaller radii where the ram pressures are higher. The same principal should hold for the inclusion of gravitational potential of the protostar.

We have also performed a set of runs to determine the effect of wind luminosity on the jet collimation. Using the results from Smith *et al.* 1983, Koo & McKee 1992 fixed the following limits on the effectiveness of hydrodynamic collimation in terms of the wind luminosity ($L_w = \frac{1}{2} \dot{M}_w V_w^2$),

$$3 < \frac{L_w}{L_{wc}} < 10 \quad (4-12)$$

In equation 4-12 L_{wc} is a critical luminosity based on, among other things, the scale height of the ambient density distribution. Since no characteristic scale exists for a power-law distribution a direct comparison with this prediction is difficult. However, we can bracket the range of luminosities where the collimation seen in our simulations operates. We have run two simulations (case G and H) with the density contrast fixed at $q = 20$ but varying the velocity from $V_w = 100 \text{ km s}^{-1}$ to $V_w = 700 \text{ km s}^{-1}$. These simulations cover a factor of 49 in the wind luminosity, nine times larger than the range predicted by equation 4-12. We find jet collimation occurs in both simulations. Thus, given the idealizations inherent in our model we find no significant limits on hydrodynamic collimation over a range of luminosities consistent with those observed in YSOs. In the next section we discuss some reasons why equation 4-12 might be wrong.

5. Collimation Mechanisms

From the results presented in the previous section it is clear that it is possible to use the interactions with the environment to produce a high degree of collimation in the shocked wind as well as transsonic flow. From these simulations and others studies of inertial collimation it appears that a number of mechanisms contribute to the production of supersonic jets. In this section we explore these mechanisms in more detail.

5.1. De Laval Nozzles

In Fig 9 we present a contour plot of model B after 300 years of evolution with cuts of velocity, pressure and Mach number along the pole plotted beneath it. As in Fig 5 the axial cuts show that immediately behind the wind shock, $R_{sw}(P)$, the flow passes through a

sonic point. We have also marked the height at which the contact discontinuity achieves a minimum width (ie $\min[r_{\text{CD}}(z)]$) in the plots shown in Fig 8. It is clear that the constriction in the walls of the shocked wind cavity occurs at the same point where the flow undergoes a sonic transition, in other words a de Laval nozzle has formed.

The presence of de Laval nozzles is not, in itself, surprising. As was noted in the introduction there is an extensive literature on de Laval nozzles as jet collimation mechanisms. Currently it appears that this type of mechanism is out of favor. But the manifestation of de Laval nozzles seen in these simulations is quite different from the standard steady state models found in the literature. Therefore the conclusions which led to the abandonment of de Laval nozzles do not apply here.

As was discussed in the previous subsection Smith *et al.* 1983 placed stringent limits on the parameter space of initial conditions under which stable de Laval nozzles were expected to form (eq 4-12). The theoretical basis for this conclusion was the expectation that beyond these limits Kelvin-Helmholtz instabilities would choke off the nozzle producing a series of bubbles rather than a continuous jet. The analytical arguments invoked were bolstered by the results of numerical simulations carried out in an earlier paper by Norman *et al.* 1981. Comparing these papers with our results is difficult because of the different initial conditions and assumptions. In spite of these differences, however, a few points can be made.

Firstly, and most obvious, the numerical simulations carried out by Norman *et al.* 1981 are highly underresolved by current standards (though they were state of the art at the time). The simulations were performed on 40×40 computational grids, which is almost a factor of 64 smaller than used in the simulations presented here. Also, one can analytically show that Kelvin-Helmholtz instabilities occur, but not that they will choke off the jet nozzle. What matters is the non-linear, time-dependent effect of the instabilities on the flow. We see in our simulations that the strong shear along the contact discontinuity does produce ripples along its surface, but rather than choke off the jet we find the instabilities end up aiding its collimation by providing the material for the dense chimney.

There is another important difference between our simulations and previous studies of de Laval nozzles. For the most part analytical investigations have assumed a steady state configuration for the nozzle by matching the pressure in the bubble with the pressure in the ambient medium (see Königl 1982 for some thoughts on the evolutionary aspects of nozzles). In our model the bubble is over pressured and keeps expanding. Here it is the inertia, not the pressure of the ambient medium which provides the basis for producing a collimating cavity. This means that if our models are to be applied to YSOs the wind or the accretion or both must be taken to be time dependent allowing the configuration to

maintain a stable average configuration. There is considerable observational support for such a conclusion as the jets themselves are known to be time dependent (Morse *et al.* 1992) We will take up this issue again in the final section.

Finally we note the issue of radiative time scales. De Laval nozzle models require the presence of high temperature gas. This has led to the conclusion that the size scales required, i.e. those of adiabatic bubbles, are too large to allow nozzles to collimate on the scales observed. However, recognition of the PRB phase discussed in Sect 3 allows de Laval nozzles to operate on considerably smaller scales than was previously thought (see also Raga & Cantó 1989). This implies that de Laval nozzles may still be an important aspect of hydrodynamic collimation mechanisms for YSO jets.

5.2. Shock Focusing

While de Laval Nozzles are clearly an important aspect of the collimation of jets in these simulations there is another mechanism at work. As was noted earlier the wind shock is not spherical. In almost all the simulations which produce jets we have found wind shock ellipticities of $0.7 < e < 0.8$ (see eq 4-5) In addition simulations of similar astrophysical systems (i.e. Planetary Nebulae, SN1987A, Superbubbles) have found stronger departures from spherical geometries with ellipticities achieved as low as $e = 0.25$ (Icke 1994, Dwarkadas *et al* 1995). When the wind shock takes on prolate geometries the radially streaming wind from the central source encounters it at an oblique angle. Only the normal component of the wind velocity will be shocked in these cases. The tangential component will remain unchanged. Thus the wind shock can act as a lens focusing the post-shock velocity vectors towards the jet axis.

In Fig 10 we present a map of the post shock velocity vectors overlaid on contours of density to show the position of the inner shock and CD. In this figure the shock has a ellipticity of $e = .79$. Note that the flow vectors close to the equator emerge from the shock without any focusing. These gas parcels are only turned towards the axis by pressure gradients at some distance downstream. But as one travels up towards the pole the flow vectors are clearly being refracted poleward *directly behind the shock*. As we shall demonstrate below flow focusing by the wind shock can be an important component of the collimation process containing the potential to produce fully supersonic jets without the presence of a de Laval nozzle.

5.3. Properties of the Inner Shock

It is difficult to make an a priori determination of the wind shock shape based only on initial conditions. The degree to which the wind shock departs from spherical symmetry will be determined by nonlinear feedback, in terms of both thermal and ram pressures, from the evolving bubble. It is not yet clear how to calculate the characteristics of this feedback analytically. Because of this difficulty almost all analytical treatments of aspherical wind-blown bubble evolution have assumed the inner shock to be spherical (see e.g. Smith *et al.* 1983, Mac-Low & McCray 1988). In contrast almost every study of these systems relying on numerical simulations has shown the inner shock to be aspherical to some degree (Mac-Low, McCray & Norman 1988, Blondin & Lundquist 1993).

Assume the shock takes on an elliptical geometry with ellipticity e defined by eq 4-5. To determine the degree of focusing in the post wind shock flow we must solve the oblique shock jump conditions. Here we repeat and extend the analysis of Icke (1988). Working in spherical coordinates, the angle (β) between the ellipse and radially directed wind will be a function of polar angle (θ) and is given by

$$\beta = \theta + \arctan\left(\frac{e^2}{\tan\theta}\right), \quad (5-1)$$

Because the wind shock is aspherical the radial distance at which the wind will encounter the shock depends on latitude. Thus the geometrical dilution of the wind will cause the pre-shock flow variables to be functions of the polar angle. We denote the pre-shock variables with the subscript “0”. Accounting for these variations we can use the jump conditions for a strong shock to express the post-shock variables (denoted with subscript “1”) as

$$v_{1p}(\theta) = \left(\frac{\gamma - 1}{\gamma + 1}\right) v_0 \sin\beta(\theta), \quad (5-2)$$

$$v_{1t}(\theta) = v_0 \cos\beta(\theta) \quad (5-3)$$

$$P_1(\theta) = P_0 \left(\frac{2}{\gamma + 1}\right) \mathcal{M}_0^2(\theta) \sin^2(\beta(\theta)) \quad (5-4)$$

$$s_1(\theta) = \left(\frac{\gamma - 1}{\gamma + 1}\right) s_0(\theta) \sqrt{\frac{2\gamma}{\gamma - 1} \mathcal{M}_0^2(\theta) \sin^2\beta(\theta) - 1}. \quad (5-5)$$

In Eqs. 5-2 through 5-5, v_{1p} and v_{1t} are the post-shock velocity parallel and tangential to the shock normal, s is the sound speed and \mathcal{M} is the Mach number. The total angle of deflection (χ) through the shock is given by

$$\tan \chi(\theta) = \frac{2 \tan \beta(\theta)}{(\gamma + 1) + (\gamma - 1) \tan \beta(\theta)} . \quad (5-6)$$

In Fig 11 we show curves of χ , P_1 , speed $v_1 = \sqrt{v_{1p}^2 + v_{1t}^2}$, and post-shock Mach number \mathcal{M}_1 as a function of polar angle for three values of the shock ellipticity e . Note that all points along the inner shock where $\chi > \theta$ have fully focused post-shock velocity vectors i.e. the flow at these points is directed towards the polar axis. For the three values of e shown all wind streamlines within $\theta_f = 30^\circ$ of the polar axis exit the shock fully focused. Here we define θ_f to be the latitude below which the flow is fully focused (i.e. $\chi = \theta$). In our simulations we found $\langle e \rangle \approx .75$ which yields $\theta_f = 33^\circ$. Thus, as Icke expressed in his original study, “even a small eccentricity causes a high degree of focusing”.

The plots of velocity demonstrate the extent to which the wind can pass through the prolate inner shock and emerge into the bubble without being significantly decelerated. In some sense a highly prolate inner shock acts much like the reconfinement shocks explored by Sanders 1983 in the context of free extragalactic jets. The plots of pressure demonstrate that additional collimation can be expected to occur as velocity vectors are turned poleward by tangential pressure gradients as is also seen in Fig 10.

The plots of the post shock Mach number \mathcal{M}_1 show that for more prolate shocks a significant region of the post-shock wind enters the bubble with supersonic velocities. Thus in principle it is in possible to produce a fully collimated supersonic jet purely through the action of shock focusing. The post shock Mach number depends upon the ratio of specific heats γ . Since we expect that shock focusing will begin during the Partially Radiative Bubble phase where the polytropic index $\gamma < \frac{5}{3}$ we have, in Fig 12, plotted $\max[M_1(\theta)]$ vs γ for 3 different ellipticities We have chosen fairly modest values of the ellipticity ($e = .5, .65,$ and $.8$) to emphasize that supersonic flows can be expected behind a wide range of inner shock configurations. Fig 11 shows that as γ decreases supersonic post shock flow can be achieved at relatively low ellipticity. In this case no de Laval nozzles are necessary to produce supersonic outflows.

6. Conclusions

The conclusions reached in this paper can be summarized as follows.

- The SFIC mechanism can, in principle, produce well collimated supersonic jets in the context of YSOs through purely hydrodynamic means.
- The SFIC mechanism requires the formation of a hot shocked bubble of gas. By considering analytical estimates of the interaction between a fast wind and its surroundings it turns out that for typical YSO parameters this condition will hold (for outflow velocities $\gtrsim 200 \text{ km s}^{-1}$). Although the bubble will not be fully adiabatic on small scales ($\sim 100 \text{ AU}$), cooling will not be efficient enough to stop the build up of a reservoir of hot gas. This partially radiative phase is quite important in the YSO case and may be in other astrophysical circumstances. A closer investigation of it would be interesting.
- The flow pattern that forms in the SFIC situation is a complex mix between wind blown bubble physics and jet physics. While the base of the jet is a reservoir of hot, subsonic gas, typical of a wind-blown bubble, the jet itself is supersonic, showing internal shocks, and a cocoon of “waste” material. It also has the characteristic jet and bow shocks, in which the bow shock in fact is identical to the outer shock of the bubble. The jet is over pressured and less dense than its environment, but since the environment does not have a constant density, the jet is expected to change to a dense one once it has moved out to larger distances. Also in its evolution the structure behaves in between what is expected from analytical estimates for bubbles and jets.
- The actual collimation in the SFIC mechanism is caused by a combination of effects. Firstly, the interaction with the surrounding medium creates a de Laval nozzle which allows a smooth transition from subsonic to supersonic flow. This nozzle is evolving and is a stable feature for a wide range of parameters in our simulations. We find none of the unstable behavior that was previously reported for these configurations. Secondly, the wind shock is aspherical which in itself leads to focusing of the outflow towards the axis. In fact, an aspherical shock may even produce super-sonic post-shock gas, since only the normal component of the velocity is shocked. For $\gamma < 5/3$ this can happen even for mildly aspherical inner shocks.

We again note that the models explored in this paper rely on the presence of an envelope of dense circum-protostellar material to produce collimated jets. Thus we feel that our results may be most relevant to the more deeply embedded class 0 objects rather than to the more evolved objects with disks such as T Tauri stars.

One may wonder about the long term evolution of these jets. We already pointed out that we expect the jets to become denser than their environment as they move out. We also pointed out that they are over pressured. This means that the whole bubble structure

expands, also laterally and that given enough time, all of the circumstellar material will be removed. For the region of parameter space explored here the time scale for this is $\sim 10^4$ years. Given the dynamical age of some HH objects it is clear that something else must occur if the mechanisms discussed here are responsible for collimating the jets. However, it is also clear that the jets are variable in time and one can envisage a situation where the outflow is temporarily stopped or weakened and the ram pressure of the accreting medium is high enough to temporarily reverse the expansion of the bubble. The jet production would, therefore, also stop. This would lead to a situation similar to the one studied by Biro & Raga 1994 in their numerical work on jets from time-dependent sources. Analytical estimates indicate that a periodic scenario of this type does indeed work (Mellema & Frank 1996b).

In the SFIC model it is unavoidable that a reservoir of hot gas forms at the base of the jet, or even that the lower part of the jet consists of high temperature gas. This material would in principle emit free-free emission, observable in the radio continuum and (soft) X-rays. However in the deeply embedded sources we are considering these X-rays might not be observable. A specific comparison with observations however is premature until more realistic physics is added. In particular the size and physical conditions in the hot cavity will strongly depend on radiative cooling thus we defer specific comparisons until these calculations have been carried out.

It is obvious that a substantial amount of work needs to be done before the SFIC mechanism can be claimed to be able to explain jets from YSOs. However given its efficiency and the fact that something like an interaction between in and outflows must take place around YSOs, we plan to explore it in some more detail in future papers. Especially the effects of cooling and the partially radiative bubble configuration will be studied in a next paper.

Acknowledgments

We wish to thank Vincent Icke, Bruce Balick, Tom Jones, Arie König, and Chris McKee for the very useful and enlightening discussions on this topic. We would also like to thank Dongsu Ryu for his generous help in making his TVD code available to us for this study. Support for this work was provided by NASA grant HS-01070.01-94A from the Space Telescope Science Institute, which is operated by AURA Inc under NASA contract NASA-26555. Additional support came from the Minnesota Supercomputer Institute.

Table 1: Initial Conditions For Runs A - H

run	M_w	V_w	M_a	q	<i>Resolution</i>
A	1×10^{-7}	200	1×10^{-5}	70	256×1280
B	2×10^{-7}	300	1×10^{-5}	70	256×1280
C	1×10^{-7}	200	5×10^{-6}	3	256×512
D	1×10^{-7}	200	5×10^{-6}	7	256×512
E	1×10^{-7}	200	5×10^{-6}	14	256×512
F	1×10^{-7}	200	5×10^{-6}	30	256×512
G	1×10^{-7}	100	1×10^{-5}	20	256×512
H	1×10^{-7}	700	1×10^{-5}	20	256×512

REFERENCES

- Balbus, S.A., 1993, ApJ, 413, L137.
- Biro, S., Raga, A., 1994, ApJ, 434, 221
- Blondin, J.M. Fryxell, B.A., & Königl A. 1990, ApJ, 360, 370
- Blondin, J.M., & Lundqvist, P., 1993, ApJ, 405, 337
- Burrows, C., & Stapelfeldt, K., 1995, in preperation
- Cantó, J., 1980, A&A ,86, 327
- Cantó, J., Tenorio-Tagle, G., Rozyczka, M., 1988, A&A 192, 287
- Camenzind, M., 1993, in “Stellar Jets and Bipolar Outflows: Proceedings of the 6th International Workshop of the IAC, eds. L. Errico and A. Vittone (Dordrecht, Kluwer), 289.
- Dal Pino, E.M.G.,1995, *1994 Conference on Plasma Physics*, AIP Publics, eds. P. Sakanaka, in press
- Dwarkadas, V., Chevalier, R.A., & Blondin, J. M., 1995, ApJ, 457, 773
- Eichler, D., 1982, ApJ, 263, 571
- Frank, A., 1992, PhD Thesis, University of Washington
- Frank, A., & Noriega-Crespo, A. 1994, A&A, 290, 643
- Galli, D. & Shu, F. H., 1993, ApJ, 417, 220
- Goodman, A.A., Bastien, P., Myers, P.C., & Ménard, F. 1990, ApJ, 359, 363.
- Hartmann, L., Boss, A., Calvet, N., Whitney, B., 1994, ApJ, 430, L49
- Hartigan, P., Morse, J.A., Heathcote, S., & Cecil, G., 1992, ApJ, 414, L121.
- Harten, A., 1983, J. Comp. Phys, 49, 357
- Heyer, M.H., Strom, S.E., & Strom, K.M. 1987, AJ, 94, 1653.
- Hirth, G.A., Mundt, R., Solf, J., 1994, A&A , 285, 929

- Holland, W. S., Greaves, J.S., Ward-Thompson, D., & Andre, P., 1995, preprint
- Icke, V., 1988, A&A, 202, 177.
- Icke, V., 1994, in “Circumstellar Matter, Proceedings of 34th Herstmoncuex conference”, eds. R. Clegg (Cambridge University Press), 210.
- Icke, V., Mellema, G., Balick, B., Eulderink, F. & Frank, A., 1992, Nat, 355, 524
- Icke, V., Balick, B., & Frank, A. 1992, A&A, 253, 224.
- Kahn, F.D., 1976, A&A, 50,145
- Kompaneets, A.S. 1960, Dokl. Akad. Nauk 130, 1001
- Koo, B., Mckee, C.F., 1992, ApJ,388, 103
- Königl, A 1982 ApJ, 261, 115
- Königl, A 1989 ApJ, 342, 208
- Mac-Low, M.M., & McCray, R., 1988, ApJ, 324, 776
- Mac-Low, M.M., McCray, R., & Norman M.L., 1988, ApJ, 337, 141
- Mellema, G., Eulderink, F., & Icke, V., 1991, A&A, 252, 718.
- Mellema, G., Frank, A., 1996, ApSS, 233, 145
- Mellema, G., Frank, A., 1996, in preparation
- Morse, J.A., Hartigan, P., Cecil, G., Raymond, J.C., & Heathcote, S. 1992, ApJ, 339, 231.
- Natta, A., & Giovanardi, C. 1990, ApJ, 356, 646
- Najita, J.R., Shu, F.H., 1994, ApJ, 429, 808
- Norman, M. L., Smarr, L., Smith, M.D., Wilson, J.R., 1981, ApJ, 247, 52
- Norman, M.L., 1993, in “Astrophysical Jets”, eds. D. Burgarella, M. Livio, & C. O’Dea, (Cambridge University Press), 210.
- Panagia, N., 1991, in “The Physics of Star Formation and Early Stellar Evolution”, eds. C.J. Lada and N.D. Kylafis, NATO ASI Series (Kluwer), 565.
- Pelletier, G., & Pudritz, R.E. 1992, ApJ, 394, 117.

- Pudritz, R.E. 1991, in “The Physics of Star Formation and Early Stellar Evolution”, eds. C.J. Lada and N.D. Kylafis, NATO ASI Series (Kluwer), 365.
- Raga, A.C. & Cantó, J., 1989 ApJ, 344 404
- Raga, A.C. & Kofman L., 1992 ApJ, 386 222
- Rodriguez, L.F., Cantó, J., 1983, Rev Mex A&A 8, 163
- Ryu, D., Brown, G.L., Ostriker, J.P., Loeb, A., ApJ, 452, 364
- Sanders, R.H., 1983 ApJ 266, 73
- Shu, F. H. 1991, in “The Physics of Star Formation and Early Stellar Evolution”, eds. C.J. Lada and N.D. Kylafis, NATO ASI Series (Kluwer), 365.
- Smith, M.D., Smarr, L., Norman, M.L., & Wilson, J.R., 1983 ApJ, 246, 432
- Stone, J.M., & Norman, M.L. 1994a, ApJ, 413, 198.
- Stone, J.M., & Norman, M.L. 1994b, ApJ, 420, 237.
- Strom, S. E., 1994, Rev. Mex. A&A., 29, 23-29
- Tenorio-Tagle, G., Cantó, J., & Rozyczka, M., 1988, A&A, 202, 256
- Tereby, S., Shu, F. & Cassen, P., 1984, ApJ, 286,529
- Todo, Y., Uchida, Y., Sato, T., & Rosner, R. 1993, ApJ, 403, 164.
- Uchida, Y., & Shibata, K. 1985, PASJ, 37, 515.
- Ulrich, R.K., 1976,ApJ, 210, 377
- Wardle, M., & Königl, A., 1993, ApJ, 410, 218.
- Weaver, R., McCray, R., Castro, J., Shapiro, P. Moore, R., 1977, ApJ, 218, 377
- Yorke, H. W.;Bodenheimer, P., Laughlin, G., 1993, ApJ, 411, 274

FIGURE CAPTIONS

- Fig. 1** Initial density distribution. Shown are the \log_{10} contours of density from eq 2-6 with an equator to pole contrast $q = 70$. The two solid lines show the angle at which $\rho = .5 \rho_{\max} = .5 \rho(90^\circ)$. These occur at $\theta \approx 45^\circ$ making the opening angle of the density distribution $\approx 90^\circ$
- Fig. 2** Transition radii as a function of velocity. Shown are the radii at which a radiative momentum driven bubble makes the transition to a partially radiative bubble (solid line) and an adiabatic bubble (dashed line). The curves are plotted for $\dot{M}_w = 10^{-7} M_\odot \text{ yr}^{-1}$, $\dot{M}_a = 10^{-6} M_\odot \text{ yr}^{-1}$ and $M = 1 M_\odot$.
- Fig. 3** Density and Velocity for Model A. Shown are a gray scale map of $\log_{10}(\rho)$ and a map of velocity vector field for model A after 1035 years of evolution. In the density map dark (light) shades correspond to low (high) densities. In the velocity field map vectors in the inner, freely expanding wind zone have not been plotted. Thus the first “shell” of vectors maps out the wind shock.
- Fig. 4** Temperature and Pressure for Model A. Shown are a gray scale map of T and P for model A after 1035 years of evolution. In the both maps dark (light) shades correspond to high (low) values. This is the reverse of the density gray scale map shown in Fig 3.
- Fig. 5** Axial plots for Model A. Shown are plots of $\log_{10}(\rho)$, velocity $\sqrt{v_r^2 + v_z^2}$, pressure P and Mach number \mathcal{M} as a function of height above the equator z . All plots are taken after 1035 years of evolution. Each plot is an average over the first 10 zones in cylindrical radius r .
- Fig. 6** Evolution of density for Model A. Shown are seven gray scale maps of $\log_{10}(\rho)$ for model A spaced 147 years apart. In the map dark (light) shades correspond to low (high) densities. Size scales are same as that shown in Figs 3 and 4.
- Fig. 7** Polar and equatorial shock evolution. In left and right upper panels the distance to the polar and equatorial ambient shocks obtained in the simulations is shown (triangles) for 9 separate times. Also shown (dashed line) are curves representing the growth predicted by analytical models of spherical self-similar bubbles. The point marked with an asterisk represents the predicted magnitude of a spherical bubble with identical input conditions as the simulation (along pole or equator). In the lower left panel an identical plot is shown for the wind shock along the equator. In the lower right hand panel the velocity of the polar ambient shock is presented (triangles). The

dashed line represents the velocity predicted for a wind blown bubble (normalized to the first data point). The solid line represents the velocity evolution for a jet. Note that the solid line can not be properly normalized to the data but its form is representative of the shape of deceleration given in eq 4-9

Fig. 8 Jet collimation and equator to pole density contrast. Shown are $\log_{10}(\rho)$ contour plots of four models which differ only in the values of equator to pole density contrast q . Upper left: Model C $q = 3$. Upper right: Model D $q = 7$. Lower left: Model E $q = 14$. Lower right: Model F $q = 3$.

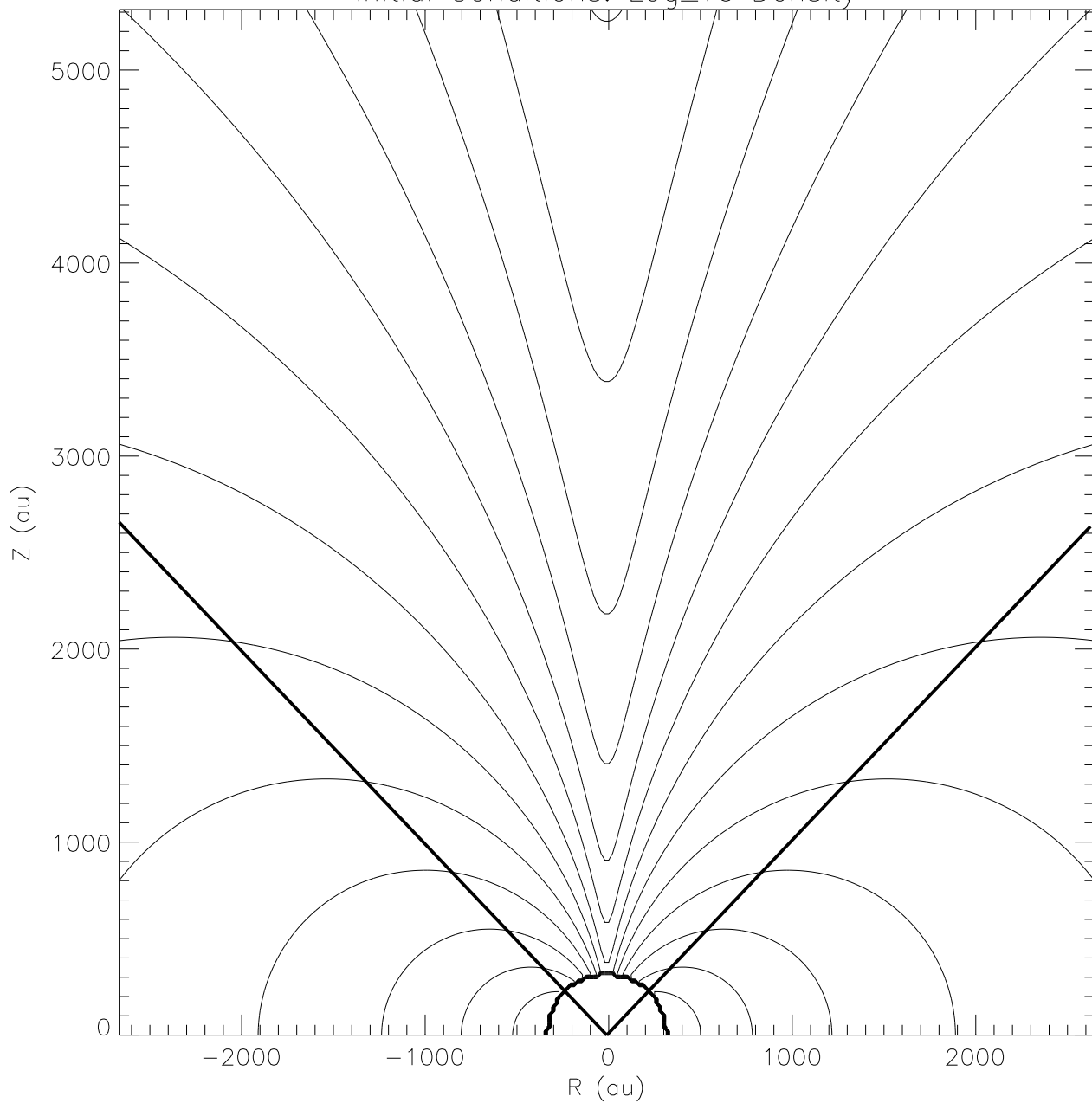
Fig. 9 De Laval Nozzles and Outflow Collimation. In the upper panel a $\log_{10}(\rho)$ contour map of model B after 750 years of evolution is shown. Below that are cuts along the z axis of velocity, pressure and Mach number. The points marked on each axial plot identify the region where the width of the channel (as measured by the contact discontinuity) has a minimum. This is the “throat” of the nozzle.

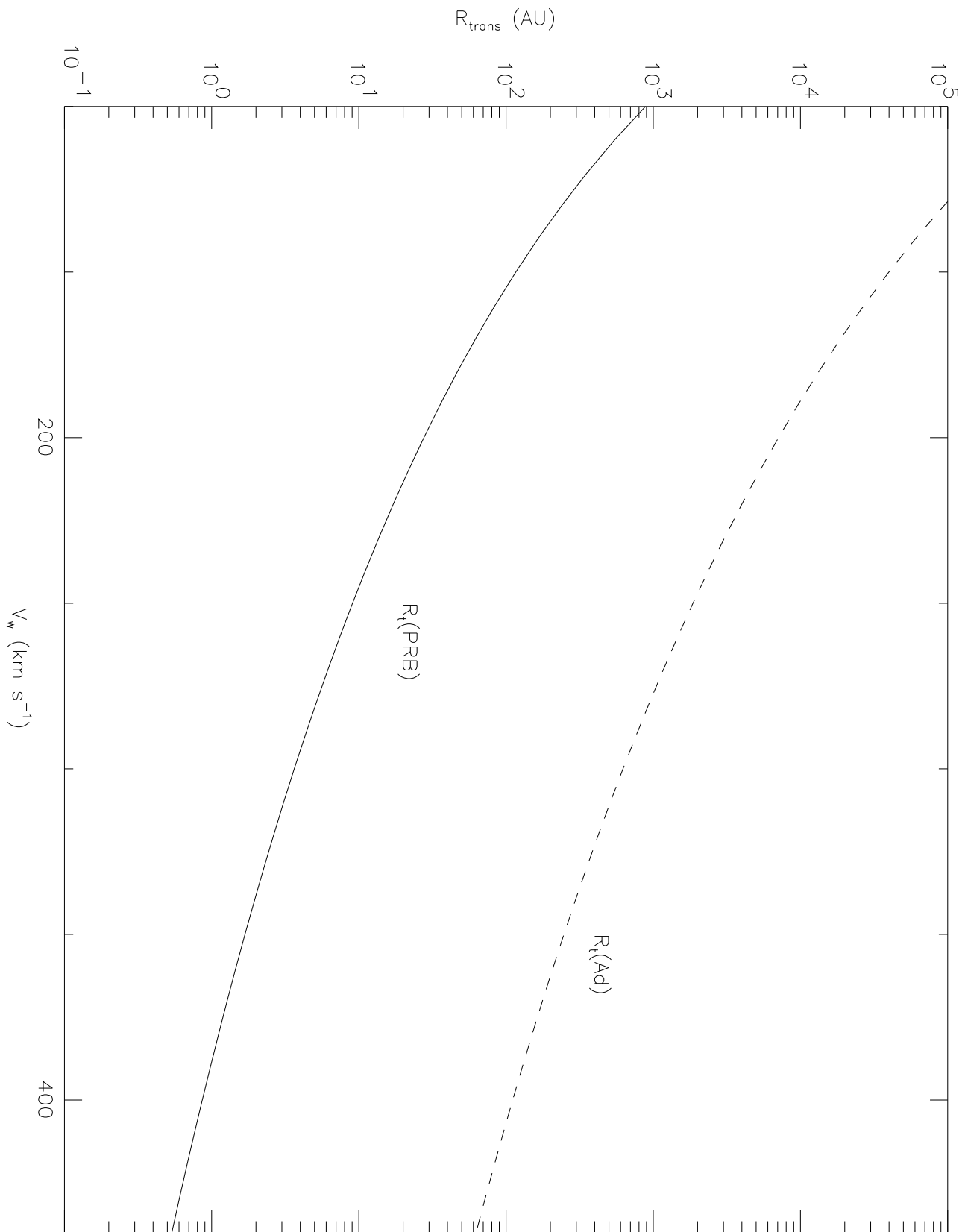
Fig. 10 Shock Focusing: Model A. Shown are selected $\log_{10} \rho$ contours identifying the wind shock and contact discontinuity. Also shown are velocity vectors for computational zones immediately downstream of the wind shock ($v < v_w$). The density contours are $\log_{10} \rho = [-20.95, -20.9, -20.85, -20.2, -20.0, -19.8, -19.6, -19.2, -19.0]$

Fig. 11 Shock Focusing: Analytical Model. Post-shock flow variables as a function of polar angle for 3 elliptical (prolate) shocks of differing ellipticity. These plots are for a wind velocity of 250 km s^{-1} and a wind density at the equator of 200 cm^{-3} . Upper left: total deflection angle. Upper right: Mach Number \mathcal{M} . Lower left: Gas Pressure P . Upper right: Velocity v . The ellipticities of the shocks are $e = .3$ (dotted line), $e = .5$ (dashed line), $e = .8$ (dash-dot line). In the plot of total deflection angle the solid line corresponds to $\chi = \theta$. All points to the left of this line have post-shock velocity vectors that are fully focused, i.e. they point towards the z axis.

Fig. 12 Post-Shock Mach Numbers for Non-Adiabatic Wind Shocks. Shown are the maximum value of the post-shock Mach number for 3 shocks of differing ellipticity as a function of the polytropic index γ . The ellipticities of the shocks are $e = .8$ (dotted line), $e = .65$ (dashed line), $e = .5$ (dash-dot line).

Initial Conditions: Log₁₀ Density



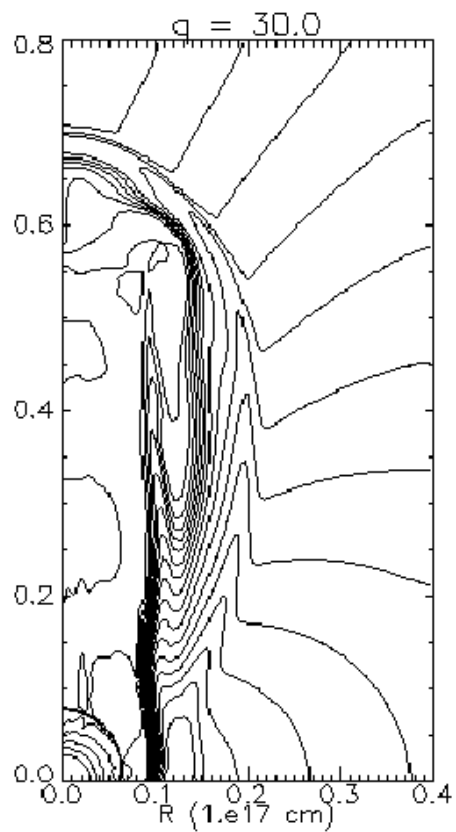
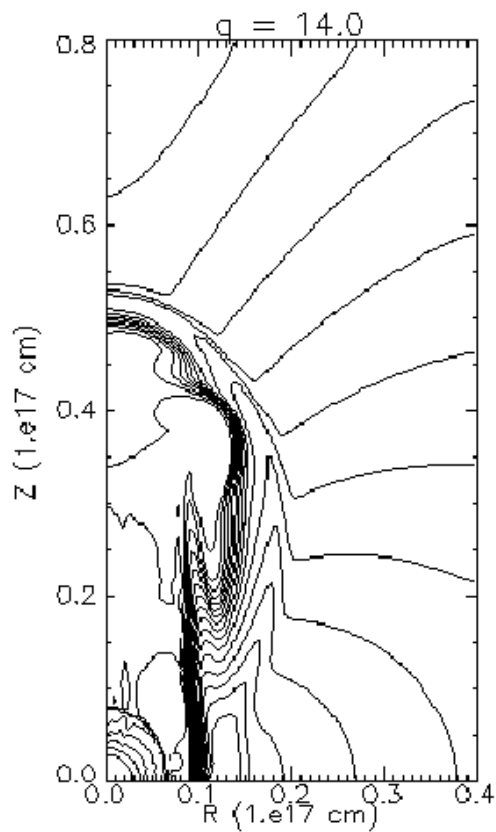
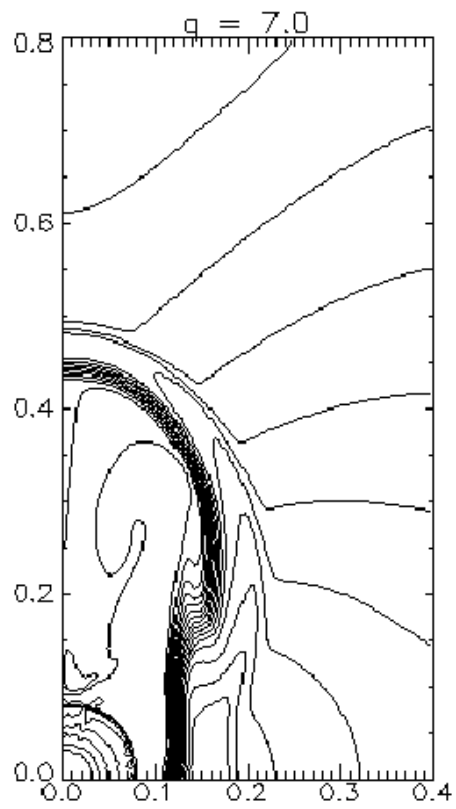
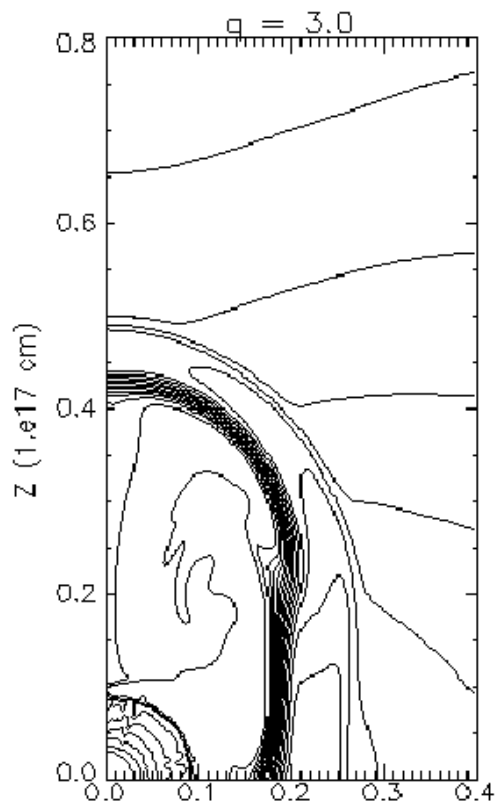


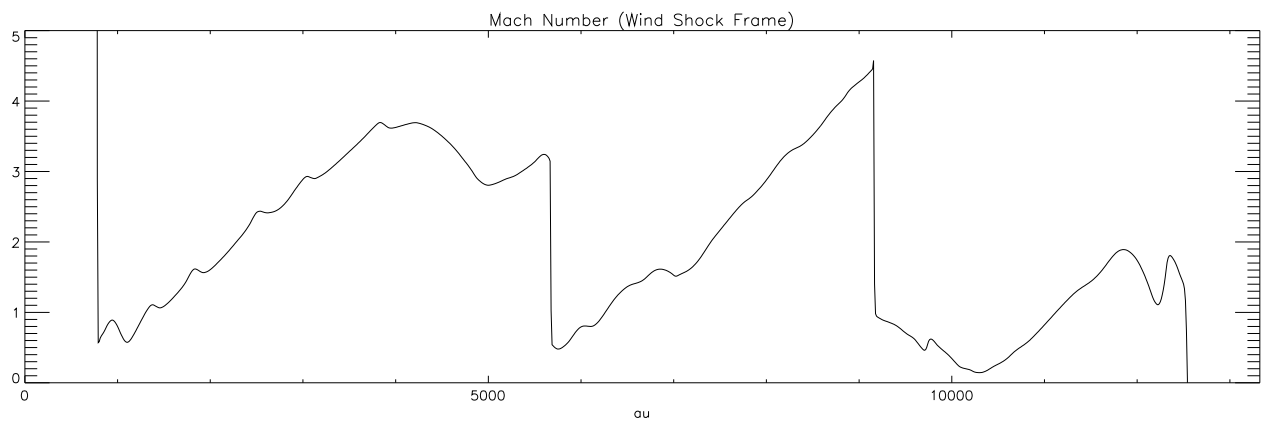
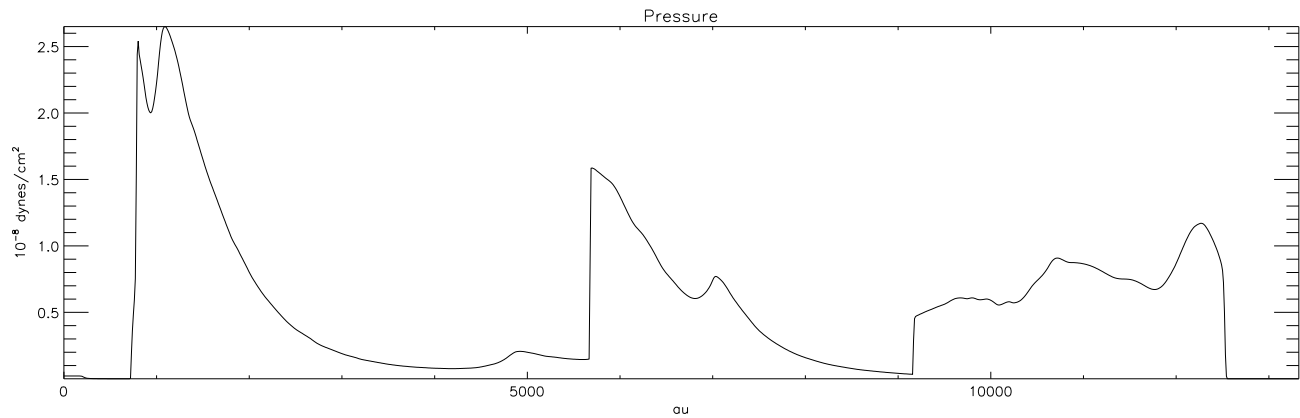
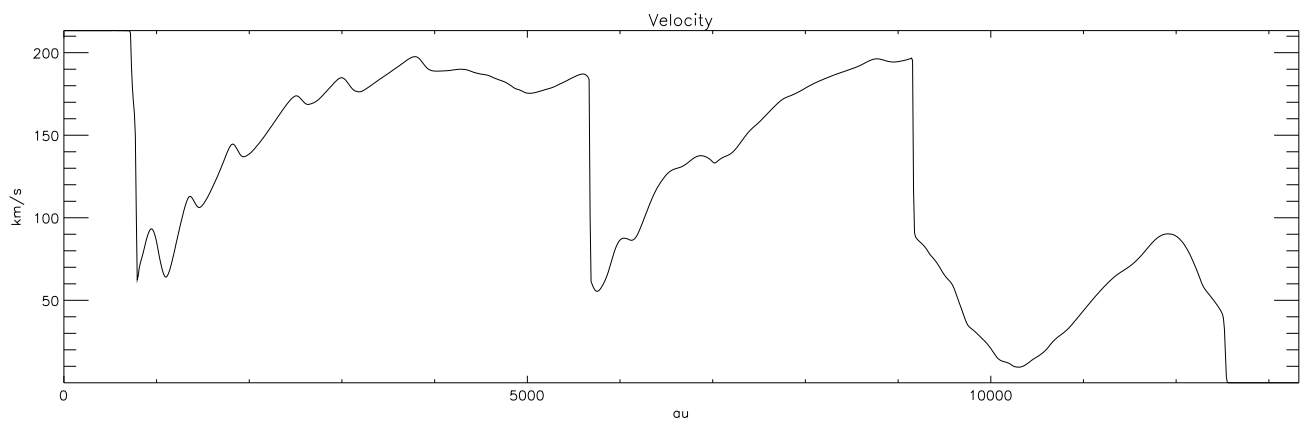
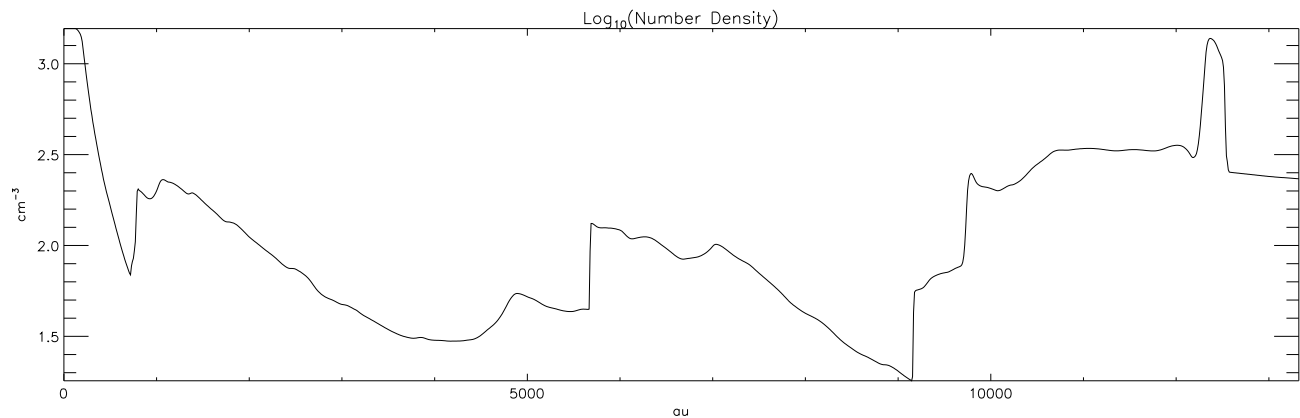
This figure "Fig3_dv.jpg" is available in "jpg" format from:

<http://arxiv.org/ps/astro-ph/9606142v2>

This figure "Fig4_tp.jpg" is available in "jpg" format from:

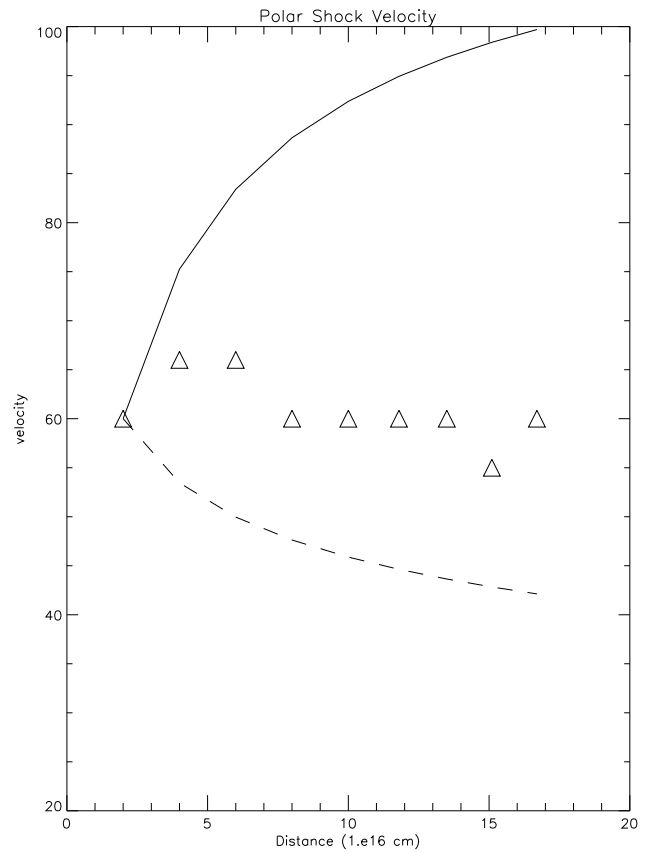
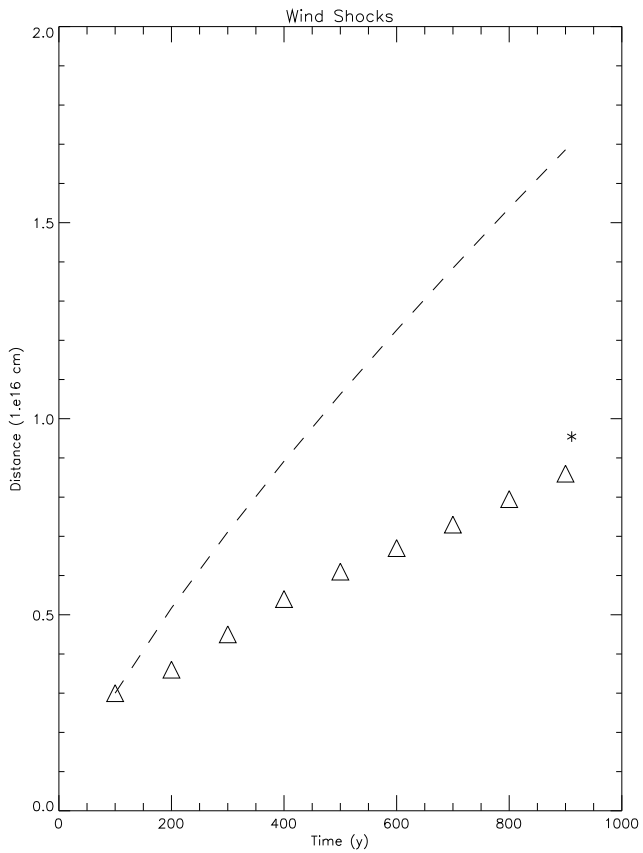
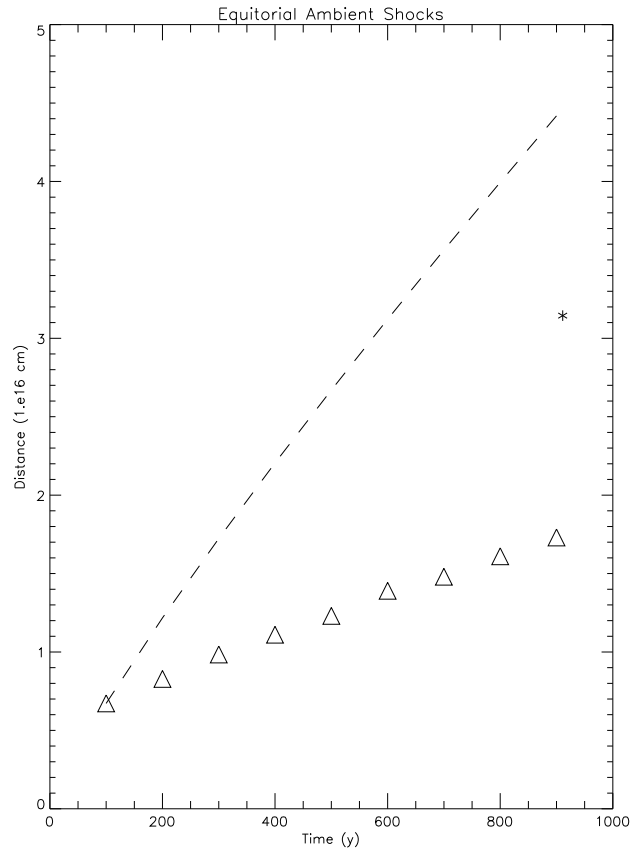
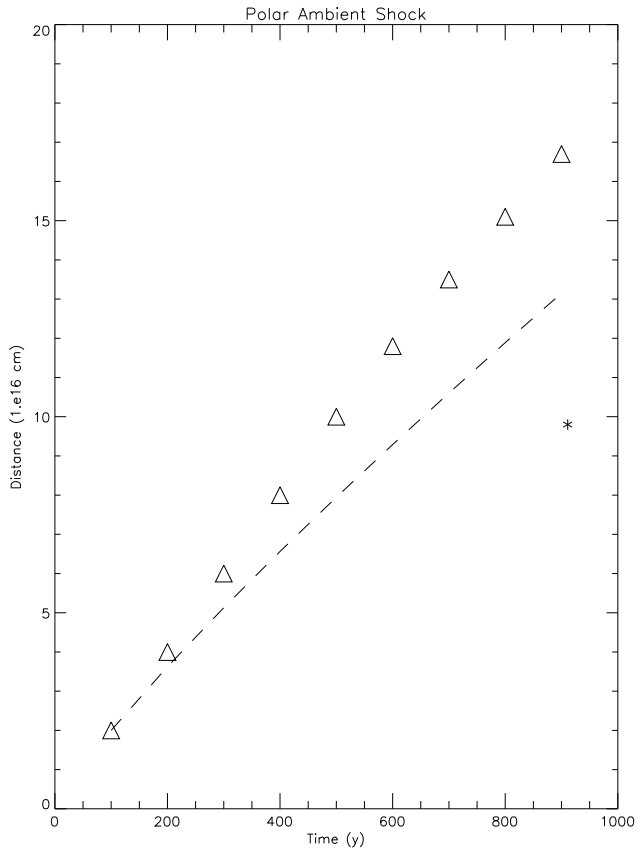
<http://arxiv.org/ps/astro-ph/9606142v2>

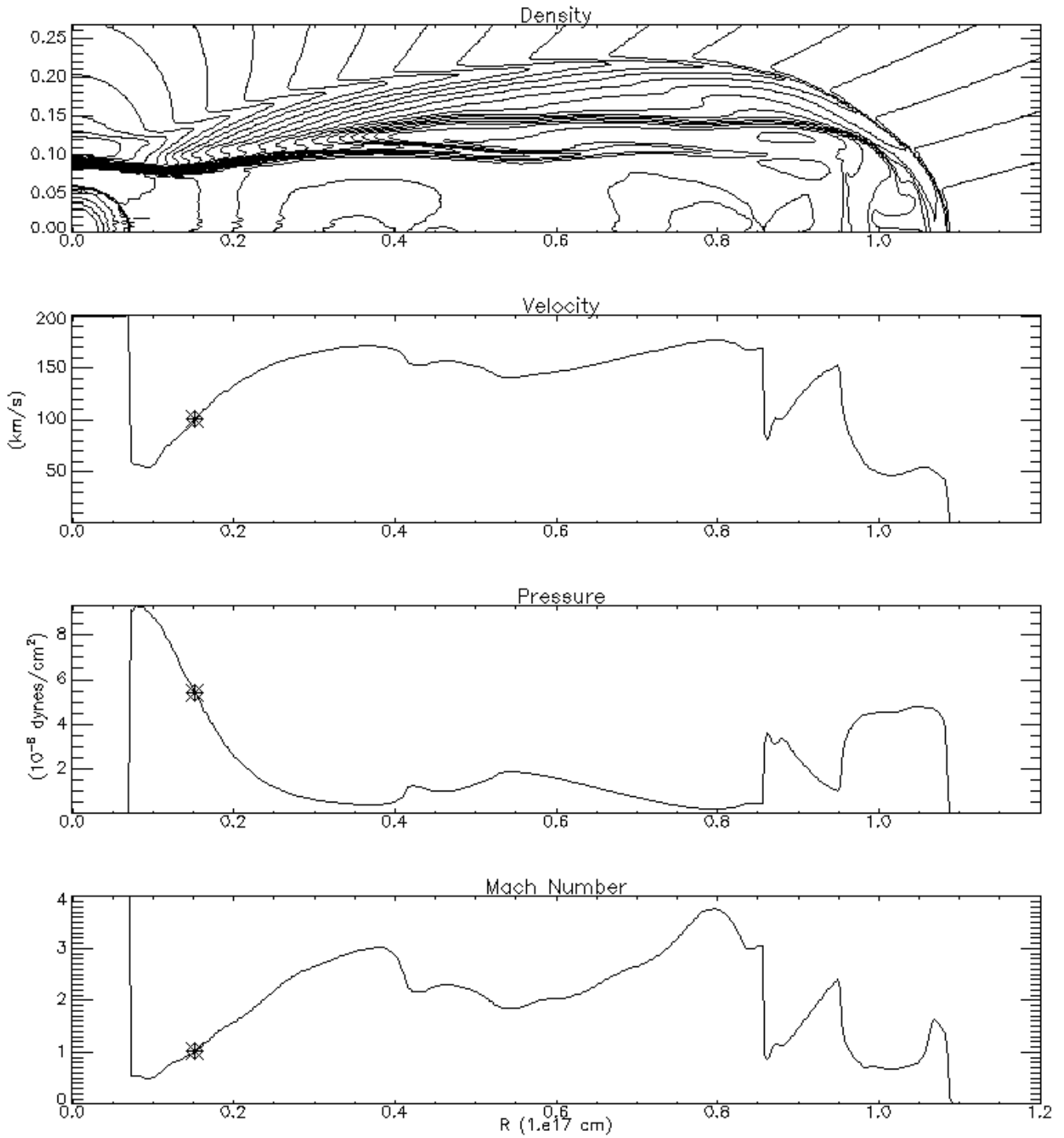




This figure "Fig6_Tser7.jpg" is available in "jpg" format from:

<http://arxiv.org/ps/astro-ph/9606142v2>





Velocity and Density

